

Dynamics of scrape-off layer filaments in detached conditions

D. Schwörer^{a,b}, N. R. Walkden^b, B. D.udson^c,
F. Militello^b, H. Leggate^a, M. M. Turner^a

^aDublin City University, Dublin 9, Ireland

^bCCFE, Culham Science Centre, Abingdon, Oxfordshire, OX14 3DB, UK

^cYork Plasma Institute, Department of Physics, University of York, Heslington, York YO10 5DQ, UK

E-mail: david.schworer2@mail.dcu.ie

18 March 2020

Abstract. The here presented work studies the dynamics of filaments using 3D fluid simulations in the presence of detached background profiles. It was found that evolving the neutrals on the time-scale of the filament did not have a significant impact on the dynamics of the filament. In general a decreasing filament velocity with increasing plasma background density has been observed, with the exception of detachment onset, where a temporarily increase in radial velocity occurs. The decreasing trend with temporary increase was found for filaments around the critical size and larger, while smaller filaments were less affected by detachment. With detachment the critical filament size increased, as larger filaments were faster in detached conditions. This breaks the trend of attached conditions, where the critical size decreases with increasing density.

1. Introduction

Filaments are field aligned pressure perturbations, observed in the tokamaks scrape-off layer (SOL), that have a much higher amplitude than the background fluctuations. They have been observed in most magnetized plasmas, including most fusion devices, where various properties of SOL fluctuations have been measured, for example the skewed probability distribution function [1–8]. In the SOL of tokamaks, filaments have been observed to cause a significant amount of transport across the magnetic field [9–11]. Filaments can be modelled non-linearly in two dimensions, evolving two fields, namely the density and the vorticity [1, 12, 13]. In this case the lack of the third dimension, parallel to the magnetic field, is typically closed by the advection closure or the sheath closure [13–17]. This has been extended in various ways in recent years, e.g. including the full parallel dynamics, which is required for capturing drift waves, and capturing sheath dynamics [13, 18, 19].

The dynamics of filaments has a dependence on their perpendicular size δ_{\perp} . While for small filaments a significant amount of the diamagnetic current across the filament is closed via currents in the drift-plane, sheath currents are important for large filaments [1, 13]. The radial velocity has a maximum at a specific size - referred to as the critical size δ^* , which represents a balance point between these two vorticity sinks.

A major challenge for the operation of fusion devices, such as ITER, is the power handling in the divertor. ITER will thus have to operate in detached, or at least partially detached conditions [20]. Detachment is an operational regime in which the heat and particle target fluxes are reduced, as a significant part of the plasma is cooled before it can reach the target [21, 22]. Detached conditions require a drop of total plasma pressure along the flux tube. Charge-exchange can be an efficient sink for plasma momentum as well as a sink for the plasma energy, reducing the heat load at the target, as well as reducing the density flux. A common condition to define detachment is the so called roll-over [20, 23]. As the upstream density is increased, during attached operation the particle target flux increases. As detachment is reached, the particle target flux drops with increasing upstream density, as a result of the loss of pressure in the vicinity of the target due to the strong interaction with the neutrals.

As detachment is reached the plasma temperature drops significantly in the vicinity of the target. This causes an increased plasma resistivity. It has been predicted that an increased resistivity results in an increased radial filament velocity [24–26]. Easy *et al* [25] found by introducing an artificially increased resistivity in addition to the increased radial velocity also an increased critical size δ^* with increasing resistivity [25]. The here presented study extends the study by Easy *et al* [25] in a self consistent way.

Filaments are a significant cross field transport mechanism and have been shown that they significantly influence the time averaged profiles [27, 28]. At the same time filaments depend on the background condition [29]. Our previous study found the importance of realistic background profiles for the dynamics of filaments, where a strong dependence of the target temperature has been observed in attached conditions [29]. In the attached conditions, only a weak influence of neutrals on the dynamic of filaments has been observed. The increased resistivity by a decreased temperature did not result in an increased velocity, as the change in target temperature had a stronger effect [25, 29]

This work aims to extend this into detached conditions, as it is expected that the filament-neutrals interaction will become important in the higher density cases. This also allows to extend the resistivity of the background plasma in a self-consistent way to levels studied by Easy *et al* [25].

The model used will be introduced in sec. 2. After a short introduction to the backgrounds profiles in sec. 3, the results of the simulations are presented in sec. 4. The simulation include the direct influence of neutrals (sec. 4.1), the impact of detachment on the radial velocity (sec. 4.2) and on the critical size (sec. 4.3) as well as the rigidity of filaments (sec. 4.4). The results will be discussed in sec. 5, before a short summary is given in sec. 6.

2. Model

STORM is a 2 fluid plasma model for the study of filaments [13, 25, 30, 31] implemented using the MPI parallelised library BOUT++ [32, 33]. BOUT++ allows a user to implement fluid models in curvi-linear geometry in close to analytical form. BOUT++ is open source, published under the LGPL license, and thus freely available ‡. STORM has recently been extended to include neutrals [29, 31].

‡ <https://boutproject.github.io/>

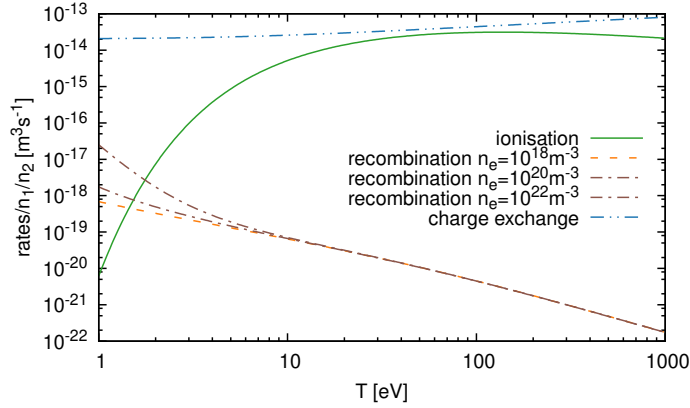


Figure 1: Temperature dependence of the neutral interaction rates Γ^{CX} , Γ^{ion} and Γ^{rec} .

Similar to the previous study, 1D background profiles, an extension of the two-point model, only retaining the parallel dimension are evolved to steady state. The 1D domain represents a flux tube, with one end representing upstream, and the other one representing the target with sheath boundary conditions. Onto the profiles the filaments are seeded and evolved.

The neutral model consists of the density of the neutrals atoms n_n , of which the logarithm is evolved. The equations are written in Bohm units, as is the rest of the STORM code [13, 29].

$$\frac{\partial \log(n_n)}{\partial t} = \frac{1}{n_n} (-\nabla_{\parallel} m_n + S_R + \Gamma^{\text{rec}} - \Gamma^{\text{ion}} + \nabla_{\parallel} \mu_{n_n} \cdot \nabla_{\parallel} n_n) - f_l \quad (1)$$

and the velocity v_n along the magnetic field lines, for which the momentum m_n is evolved

$$\begin{aligned} \frac{\partial m_n}{\partial t} = & -\nabla_{\parallel} v_n m_n - \nabla_{\parallel} n_n T_n + \Gamma^{\text{rec}} U \\ & + \Gamma^{\text{CX}}(U - v_n) - \Gamma^{\text{ion}} v_n + \mu_{m_n} \nabla_{\parallel}^2 m_n - S_R v_{th} \end{aligned} \quad (2)$$

The charge exchange, ionisation and recombination rates are denoted by Γ^{CX} , Γ^{ion} and Γ^{rec} respectively. The temperature dependence is shown in fig. 1. U denotes the ion parallel velocity. The model is similar to the UEDGE fluid model [34]. As the plasma flows are strongly field aligned, evolving the parallel velocity of the neutrals allows to model the friction in a momentum conserving way. As the background are only one dimensional, the inclusion of perpendicular velocities of the neutrals would thus have no impact on the backgrounds. $S_R(x, y, z_{\parallel}, t) \propto \exp(-(z_{\parallel} - z_t)^2 / l_R^2) \cdot n_t U_t$ is the source due to recycling, which is a Gaussian function located at the target $z_{\parallel} = z_T$ with falloff length l_R of 0.1 m. The integral $\int S_R dz = 0.99 n_t U_t$ sums to 99% of the particle target flux $n_t U_t$. μ_{n_n} is the neutral diffusion, and f_l is a loss fraction, compensating the lack of cross-field losses. The temperature of the neutrals T_n is not evolved, and is assumed to be 3 eV, close to the Franck-Condon energy [35], with the associated thermal speed v_{th} . Evolving the logarithm of the density, rather than the density itself is beneficial for the stability of the code. As the neutral density can vary quite strongly within a small spatial region, this is of importance for running

simulation in detached conditions. The logarithm further ensures that the density-solution always remains positive. Using the logarithm also changes the error norm, which matters as an iterative solver (PVIDE) is used to evolve the system. Using the logarithm increases the accuracy in the presence of low densities. For the recycling, in previous models an exponential function $S_R \propto \exp((z_{\parallel} - z_t)/l_R)$ was chosen. As a small recycling falloff length l_R is preferred to model the recycling in detached conditions, this caused a strong finite-size dependence, as the gradient is highest next to the target, thus refining the grid causes the neutrals to be deposited increasingly close to the the target. This is avoided by switching to a Gaussian function. It still retains the strong drop-off further away from the target. As later shown in fig. 4, the strong gradients near the sheath boundary conditions, due to detachment, need to be resolved. Thus the mesh contained 480 points in parallel direction, giving a uniform grid spacing of ≈ 2.1 cm, significantly refined compared to previous studies [13, 29].

The geometry used is a simple slab geometry, with x being the radial coordinate, z being the parallel direction, and y being the bi-normal direction. Only half of the flux tube is simulated, thus symmetry boundary conditions are used at the mid-plane [29]. At the target sheath boundary conditions are applied, requiring the ion velocity to reach the speed of sound c_s , and the electrons $c_s \exp(-V_f - \frac{\phi}{T})$ with the floating potential $V_f = \frac{1}{2} \log\left(\frac{2\pi}{\mu}\right)$ and the ion-electron mass ratio is $\mu = m_i/m_e$.

The STORM equation describing the plasma consist of the density n equation for the electrons

$$\frac{\partial n}{\partial t} = \frac{\nabla\phi \times \vec{b}}{B} \cdot \nabla n - \nabla_{\parallel}(Vn) + \mu_n \nabla^2 n - gn \frac{\partial \phi}{\partial y} + g \frac{\partial nT}{\partial y} + \Gamma^{\text{ion}} - \Gamma^{\text{rec}} \quad (3)$$

where ϕ denotes the potential, which is the Laplacian inversion $\omega = \nabla_{\perp}^2 \phi$ of the vorticity. The magnetic field is of direction $\vec{b} = \hat{z}$ and of magnitude $B = 0.5$ T. μ_{α} is the diffusion rate for quantity α , so μ_n denotes the diffusion rate for the density. g is the effective gravity constant playing the role of magnetic curvature. g is related to the major radius R_c which is set to 1.5 m thus $g = \frac{2}{R_c} \approx 1.33 \text{ m}^{-1}$. Both R_c and B were chosen to be representative of MAST. The terms containing g are drive terms. The equation for the parallel electron velocity V is given by

$$\begin{aligned} \frac{\partial V}{\partial t} = & \frac{\nabla\phi \times \vec{b}}{B} \cdot \nabla V - V \nabla_{\parallel} V + \mu \nabla_{\parallel} \phi - \frac{\mu}{n} \nabla_{\parallel} nT \\ & + n\mu\eta_{\parallel}(U - V) - 0.71\mu \nabla_{\parallel} T - \frac{V}{n} \Gamma^{\text{ion}} + \mu_{\parallel} \nabla_{\parallel}^2 V \end{aligned} \quad (4)$$

The parallel ion-electron resistivity is given by η_{\parallel} . Electron neutral collisions are neglected, as they only become important below 1 eV [25]. The viscosity term μ_{\parallel} was introduced to improve the numerical stability, with the magnitude $\hat{\mu}_{\parallel} = 1600 \text{ m}^2 \text{ s}^{-1}$ or in Bohm units $\mu_{\parallel} = 20$ well below the Braginskii level [36]. The equation for the parallel ion velocity U is given by

$$\begin{aligned} \frac{\partial U}{\partial t} = & \frac{\nabla\phi \times \vec{b}}{B} \cdot \nabla U - U \nabla_{\parallel} U - \nabla_{\parallel} \phi - \eta_{\parallel} n(U - V) \\ & + 0.71 \nabla_{\parallel} T - \frac{U}{n} \Gamma^{\text{ion}} - \frac{U}{n} \Gamma^{\text{CX}} + \mu_{\parallel} \nabla_{\parallel}^2 U \end{aligned} \quad (5)$$

the equation for the electron temperature T is given by

$$\begin{aligned} \frac{\partial T}{\partial t} = & \frac{\nabla\phi \times \vec{b}}{B} \cdot \nabla T - V\nabla_{\parallel}T + \frac{2}{3} \left(\frac{-1}{n} \nabla_{\parallel}q_{\parallel} + 0.71(U - V)\nabla_{\parallel}T - T\nabla_{\parallel}V \right. \\ & \left. + \frac{\kappa_{\perp}}{n} \nabla_{\perp}^2 T + \eta_{\parallel}n(U - V)^2 + \mu_{\parallel} \frac{V}{n} \nabla_{\parallel}^2 V \right) - \frac{2}{3}gT \frac{\partial\phi}{\partial y} - \frac{2}{3}g \frac{T^2}{n} \frac{\partial n}{\partial y} - \frac{7}{3}gT \frac{\partial T}{\partial y} \\ & - \frac{2}{3}gV^2 \frac{1}{\mu n} \frac{\partial nT}{\partial y} - \frac{T}{n} \Gamma^{\text{ion}} - \frac{T}{n} \Gamma^{\text{CX}} - \frac{1.09T - 13.6eV}{n} \Gamma^{\text{rec}} - \frac{30eV}{n} \Gamma^{\text{ion}} - R^{\text{imp}} \end{aligned} \quad (6)$$

The parallel heat conduction is given by q_{\parallel} and κ_{\perp} is the perpendicular heat transport coefficient. The impurity radiation R^{imp} is using the carbon radiation model from Hutchinson [21] using an impurity fraction of 1%. The radiation seems to have only a minor impact, and is not responsible for the total plasma pressure drop in front of the target. The equation for the vorticity ω is given by

$$\frac{\partial\omega}{\partial t} = A_{\omega} + J_{\omega} + B_{\omega} + C_{\omega} + N_{\omega} \quad (7)$$

$$A_{\omega} = \frac{\nabla\phi \times \vec{b}}{B} \cdot \nabla\omega - U\nabla_{\parallel}\omega \quad (8)$$

$$J_{\omega} = \nabla_{\parallel}(U - V) + \frac{U - V}{n} \nabla_{\parallel}n \quad (9)$$

$$B_{\omega} = \mu_{\omega} \nabla^2\omega + \nabla_{\perp}\mu_{\omega} \cdot \nabla_{\perp}\omega \quad (10)$$

$$C_{\omega} = \frac{g}{n} \frac{\partial nT}{\partial y} \quad (11)$$

$$N_{\omega} = -\frac{1}{n} \nabla_{\perp}^2\phi(\Gamma^{\text{CX}} + \Gamma^{\text{ion}}) - \frac{1}{n} \nabla_{\perp}\phi \cdot \nabla_{\perp}(\Gamma^{\text{CX}} + \Gamma^{\text{ion}}) \quad (12)$$

with A_{ω} the advective contribution of the vorticity equation, J_{ω} the one arising from the current, B_{ω} the diffusive and N_{ω} the contribution due to neutral plasma interaction. The curvature drive terms are C_{ω} . ω gives the potential ϕ using the Boussinesq approximation

$$\omega = -\nabla_{\perp}^2\phi \quad (13)$$

with the viscosity μ_{ω} given by

$$\mu_{\omega} = (1 + 1.6q^2) \frac{6}{8} \frac{\rho_i^2 n Z^4 \Lambda}{\sqrt{m_i} \epsilon_0^2 3(2\pi T_i)^{1.5}} \propto \frac{n}{T^{\frac{1}{2}}} \quad (14)$$

The cross field transport coefficients are calculated self consistently, following the derivation of Fundamenski *et al* [29,37]. Further details about the model are given in reference [29]. The neutral terms in the vorticity equation (7) provide a sink for the drive. In order to derive a scaling for this sink, we follow the common approach and balance the drive term with the neutrals sink [14, 16, 17, 30, 38–40]:

$$\frac{g}{n} \frac{\partial nT}{\partial y} \sim \frac{1}{n} \nabla_{\perp}^2\phi(\Gamma^{\text{CX}} + \Gamma^{\text{ion}}) + \frac{1}{n} \nabla_{\perp}\phi \cdot \nabla_{\perp}(\Gamma^{\text{CX}} + \Gamma^{\text{ion}}) \quad (15)$$

Replacing derivatives by the inverse filament size

$$g \frac{\delta_p}{\delta_\perp} \sim \frac{\phi (\Gamma^{\text{CX}} + \Gamma^{\text{ion}})}{\delta_\perp^2} \quad (16)$$

with the pressure perturbation δ_p

$$\phi \sim \delta_p \frac{g \delta_\perp}{\Gamma^{\text{CX}} + \Gamma^{\text{ion}}} \quad (17)$$

we get the filament velocity

$$v_r \sim \delta_p \frac{g}{\Gamma^{\text{CX}} + \Gamma^{\text{ion}}} \quad (18)$$

Thus if the curvature drive is balanced mainly by the neutrals, the filament velocity should have no size dependence $v_r \propto \delta_\perp^0$. For filaments in the viscous regime, where the drive is balanced by viscosity, a scaling of $v_r \propto \delta_\perp^2$ is expected [41]. In the inertial regime, a scaling of $v_r \propto \delta_\perp^{\frac{1}{2}}$ is expected, and in the sheath limited regime, a scaling of $v_r \propto \delta_\perp^{-2}$ is expected, thus the neutral scaling lies between the inertial and sheath limited regime, and is expected to be the dominant closing mechanism for large filaments, that are not able to connect to the sheath.

The different contribution of the vorticity can be either stored during the simulation, or calculated as part of the post-processing. The new python interface for BOUT++ allows to use exactly the same numerical implementation, that was used during the simulation in the post-processing scripts [42]. This results in several 4D data sets that have to be compared. By restricting to the analysis to $t = t_{\text{peak}}$ where the filaments are fastest, restricts the data set to 3D. The structure of the contribution in the perpendicular plane is of interest [30]. In order to further reduce the the amount of data, each 2D slice d in the perpendicular plane was projected onto a set of physically motivated basis vectors $e_{i,j}$. The basis vectors $e_{i,j}$ are centred on the centre of mass of the filament, and periodicity in y was taken into account such that the branch-cut was at $y_{\text{cut}} = c_y \pm \frac{1}{2}L_y$. The first 3 base vectors

$$e_{0,0} = \sqrt{\frac{2}{\pi}} \delta_\perp^{-1} e^{-\frac{x^2+y^2}{\delta_\perp^2}} \quad (19)$$

$$e_{1,0} = \sqrt{\frac{2}{\pi}} \frac{2x}{\delta_\perp} \delta_\perp^{-1} e^{-\frac{x^2+y^2}{\delta_\perp^2}} \quad (20)$$

$$e_{0,1} = \sqrt{\frac{2}{\pi}} \frac{2y}{\delta_\perp} \delta_\perp^{-1} e^{-\frac{x^2+y^2}{\delta_\perp^2}} \quad (21)$$

are shown in fig. 2

The data d can be projected onto the basis vectors, thus we get the data components $d_{i,j}$ for each slice in z :

$$d_{i,j}(z) = e_{i,j} \cdot d = \int \int e_{i,j}(x,y) d(x,y,z) dx dy \quad (22)$$

Probably the most interesting component is the (0,1) component which represents a dipole in bi-normal direction. This creates an $E \times B$ force in the radial direction,

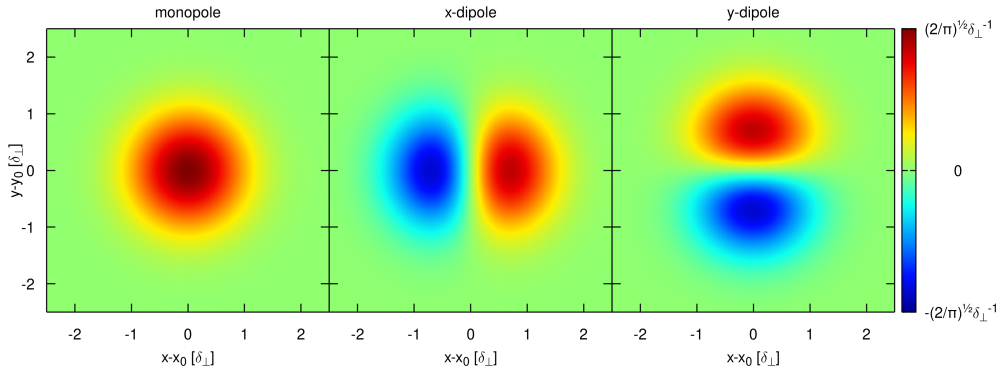


Figure 2: The first three base vectors, representing monopole, radial bipole and bi-normal dipole.

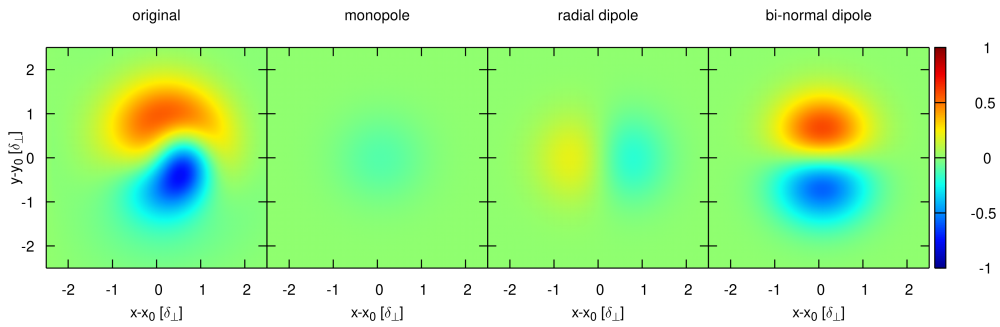


Figure 3: Some 2D simulation data and its projection on the three base vectors shown in fig. 2. Rather than the projection itself, the projection multiplied by the basis vector is shown. All quantities are plotted on the same scale. It can be seen that the monopole contribution is rather weak, with $-3.0e_{0,0}$ a.u. The radial contribution is larger with $-5.9e_{1,0}$ a.u. while the bi-normal contribution is the largest one with $18e_{0,1}$ a.u.

and is thus related to the radial drive. The other two moments that have been analysed are the (0,0) component, that represents the monopole contribution, and the (1,0) component, that in turn describes a dipole in radial direction. A monopole in the vorticity field is causing a monopole potential, and thus via $E \times B$ a spinning motion [30]. The (1,0) component, or dipole in radial direction causes a motion in bi-normal direction. Fig. 3 shows the decomposition of some data, that would represent a single point in the later discussed fig. 13 in each of the three plots for monopole, bi-normal dipole and radial dipole.

After the backgrounds have been calculated, the neutral-plasma interaction was modified in the filament simulations, to study the filament-neutrals interaction in more detail. In the “full neutral” model, the neutrals are evolved, using the equations above, and the interaction rates Γ^α are calculated self consistently. In the “static neutral” model, the neutrals are kept at their steady state values as determined by the background calculations, and the interaction rate Γ^α are calculated based on plasma and neutral distribution. In the “no interaction” model, the neutral contribution to the vorticity equation is dropped.

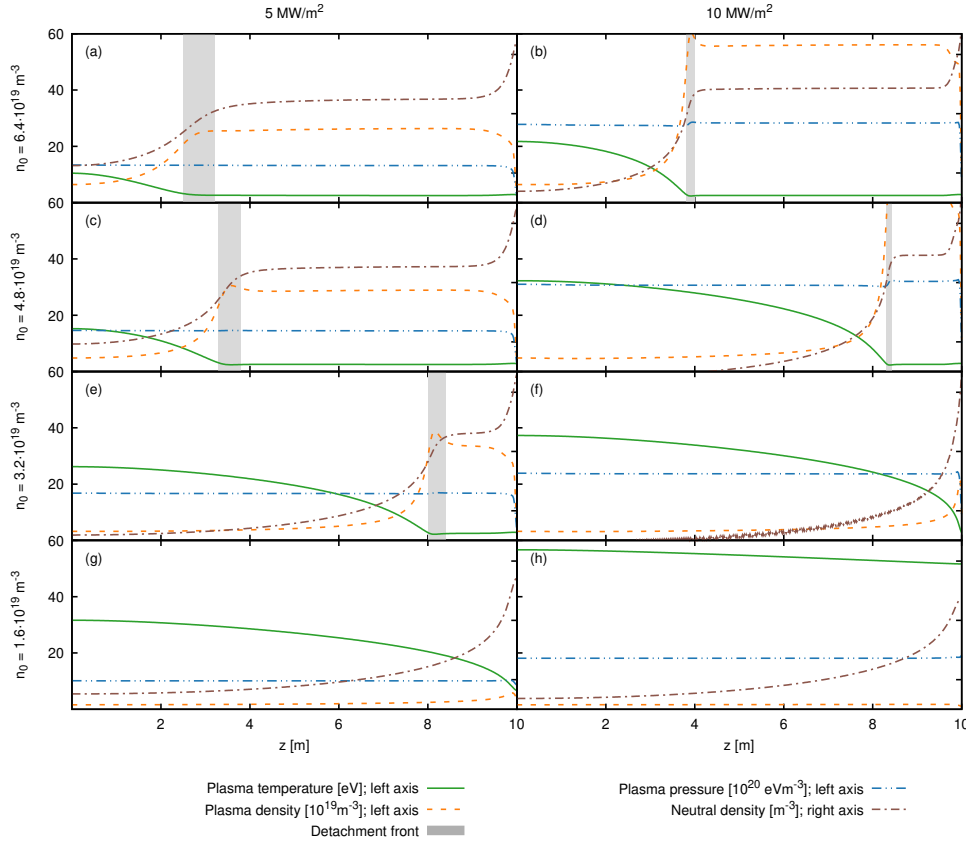


Figure 4: Background plasma profiles, run to steady-state for a set energy influx P_i and density n_0 . The sheath is at the right hand side at $L = 10$ m. The mid-plane is at the left side, and is a symmetry plane. The scales are kept the same in all subplots, to allow an easy comparison of the differences. Plasma density n_p (green line) in units of 10^{19} m^{-3} and temperature T (orange dashed) in units of eV is plotted to the linear scale on the left hand side. The neutral density n_n (brown dash dotted) is plotted to the log scale on the right hand side. Plasma pressure p_n (blue dash double dotted) in units of $2 \cdot 10^{19} \text{ eVm}^{-3}$ is the sum of static plasma pressure $n_p T$ and dynamic pressure nU^2 , plotted on the linear scale on the left. On the left hand side of the plot are simulations with an energy influx of 5 W/m^2 , right are profiles with an energy influx of 10 W/m^2 . The upstream densities n_0 are bottom to top $n_0 = 16 \cdot 10^{18}, 32 \cdot 10^{18}, 48 \cdot 10^{18}$ and $64 \cdot 10^{18} \text{ m}^{-3}$. The detachment front is highlighted by a shaded area. Fig. 5 provides a zoom-in of the last m in front of the target.

3. Background profiles

In order to run the filament simulations, 1D backgrounds along the parallel direction were computed using the equations described in section 2. An upstream energy source is included which is exponentially shaped and located at the mid-plane, as well as a Gaussian density source, which is also located at the mid-plane. The density source was controlled in such a way that a predefined density value upstream was achieved. The energy influx is set to values in the range of 5 MW/m^2 to 10 MW/m^2 and the 1D simulation were run to steady state. Fig. 4 shows some of the obtained backgrounds.

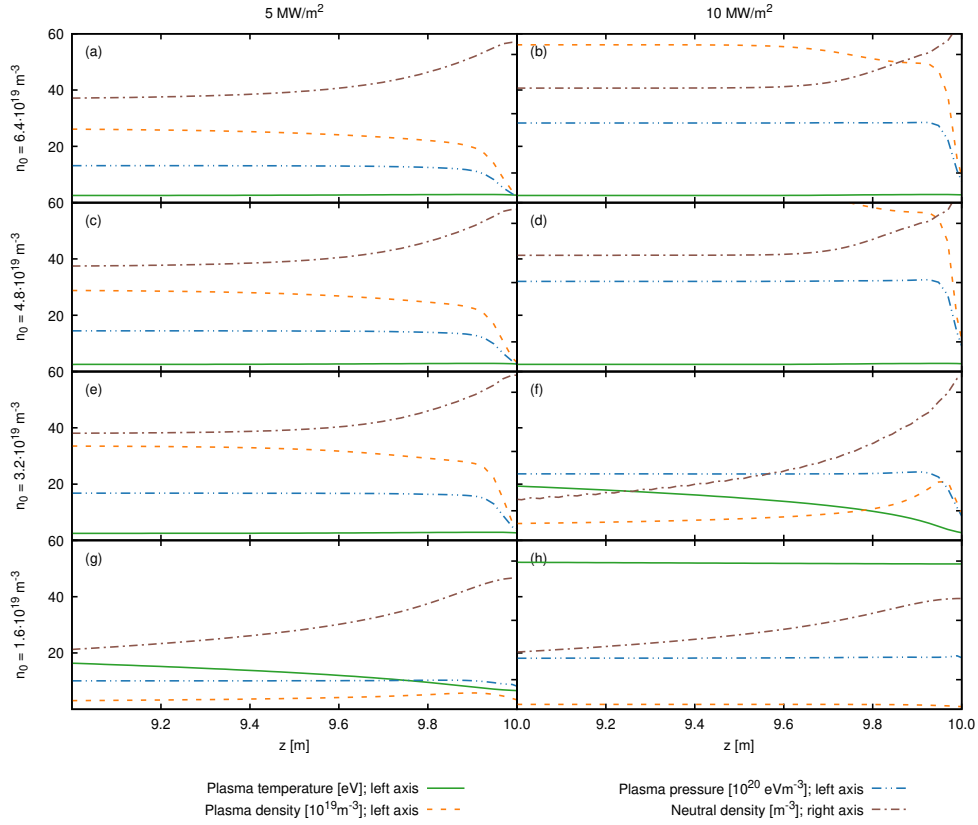


Figure 5: Zoom-in of the last m in front of the target of fig. 4. See fig. 4 for details.

With the exception of the bottom right figure, a significant temperature drop towards the target is observed. The plasma pressure, plotted with a blue dashed double dotted line stays mostly constant, until shortly before the target. The target pressure in fig 5 (a,c) drops to 20 % of the upstream value, while in (g) the pressure stays basically constant along the flux tube, while in (b) the pressure drops to around $\frac{1}{3}$ of the upstream value. As the upstream plasma density increases, the region of increased neutral density extends along the field line, where the plasma temperature is low, and the plasma density is increased. As long as the pressure stays constant, a decrease in plasma temperature coincides with an increase in plasma density to conserve pressure. 0.5 m in front of the target the neutral density increases further, which causes the plasma pressure to decrease several cm in front of the target. The dependence of the particle target flux on the upstream density is shown in fig. 6. For the 7 and 10 MW/m² cases the particle target flux increases initially before it decreases for higher densities. In the 5 MW/m² case the roll-over happens below $24 \cdot 10^{18} \text{ m}^{-3}$. This means that most of the 5 MW/m² cases are detached, while only the higher density cases at 10 MW/m² are detached. Detachment on-set, featuring pressure drop, is indicated by the shaded areas for the respective energy influxes.

While this code produces detached solutions, the details may vary compared to more complex codes, such as SOLPS, due to the additional neutral physics, as for

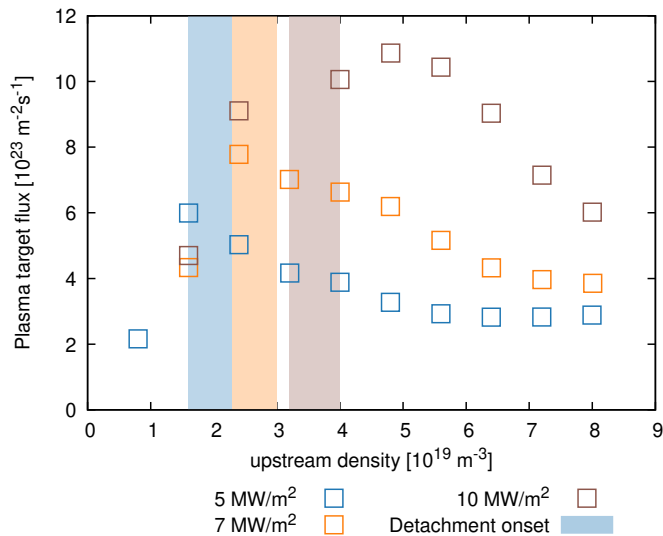


Figure 6: Particle target flux roll-over plot for different energy influxes, obtained with the described 1D model. Some of the profiles are shown in fig. 4. The shaded area represent detachment onset, according to the onset of pressure drop.

example no molecules are included, or the lack of the 2nd or 3rd dimension [22]. Further kinetic neutral effects, molecular effects, as well as effects due to a full geometry are neglected. As the three main interaction between plasma and neutrals are included, namely charge exchange, ionisation and recombination, It is expected that this model still captures the general trend and as it is the first study of interaction between filaments and detachment provides motivation for further, more complete studies. Thus the results are not expected to accurately predict experimental observation, but capture the lowest order effect of detachment on filament dynamics and thus give qualitative useful results concerning the phenomenology of filament motion in detached conditions.

4. Filament evolution

Filaments were seeded on the backgrounds discussed in sec. 3. They were seeded as a Gaussian perturbation in the drift plane, and with a tanh shape in the parallel direction, where the length was chosen as 5 m. In the perpendicular direction a Gaussian width of 2 cm was chosen for the initial studies [29], which was later varied to study the role of δ_{\perp} .

The perturbation for density and temperature was chosen equal to the upstream background value n_0 and T_0 . This keeps the relative perturbation $\frac{\delta n}{n_0}$ as well as $\frac{\delta T}{T_0}$ in all cases upstream constant, at $\frac{\delta n}{n_0} = \frac{\delta T}{T_0} = 1$.

The filament was evolved and the centre of density was tracked in the drift plane by taking the centre of mass above a threshold. This is described in more detail in our previous paper [29].

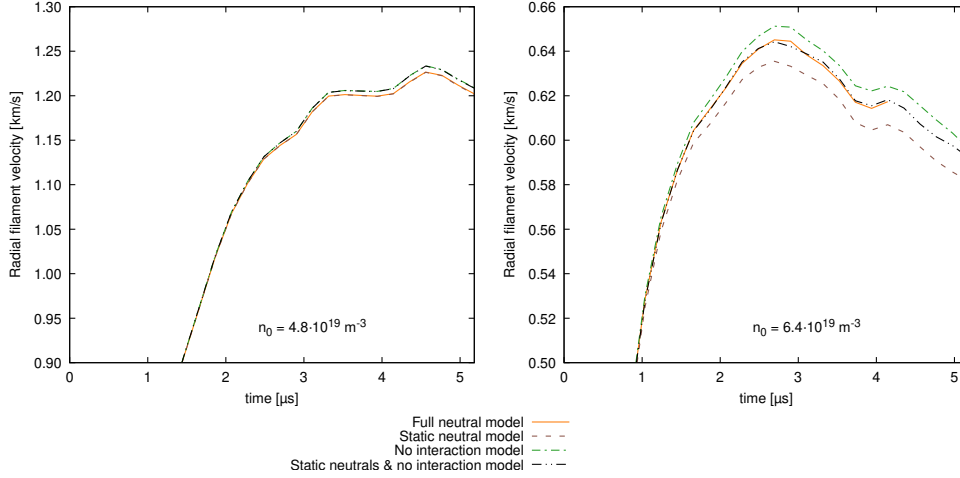


Figure 7: Time evolution of the radial velocity of a filament seeded on the background with 10 MW/m^2 and $n_0 = 48 \cdot 10^{18} \text{ m}^{-3}$ (left) as well as $n_0 = 64 \cdot 10^{18} \text{ m}^{-3}$ (right), shown in fig. 4(d,b). Results for different neutrals model are shown, see legend. The initial acceleration is not shown to make the differences between the models more visible.

4.1. Direct influence of neutrals

Fig. 7 shows the time evolution of the radial velocity of a filament seeded on the high density backgrounds $n_0 = 48 \cdot 10^{18} \text{ m}^{-3}$ and $n_0 = 64 \cdot 10^{18} \text{ m}^{-3}$ in the 10 MW/m^2 case, shown in fig. 4(b,d). The no-interaction models in all cases show higher radial filament velocity than the version that includes the vorticity-neutral interaction, however the effect is below 1% in the $n_0 = 64 \cdot 10^{18} \text{ m}^{-3}$ case and not noticeable in the lower density cases.

In the $n_0 = 48 \cdot 10^{18} \text{ m}^{-3}$ case, keeping the neutrals static decreases the velocity by less than 0.1%. In the $n_0 = 64 \cdot 10^{18} \text{ m}^{-3}$ case where the cold detachment front is within the seeded filament, the static neutral simulation over-estimates the influence of the neutrals, resulting in a decreased radial filament velocity by about 1.5%. This can be explained by looking at the plasma profiles, shown in fig. 8. In the $n_0 = 48 \cdot 10^{18} \text{ m}^{-3}$ case the cold plasma region does not extend into the seeded filament, and thus the neutral density is rather low in the seeded filament. In the $n_0 = 64 \cdot 10^{18} \text{ m}^{-3}$ case, the filament is seeded within the cold plasma region which includes a high neutral density. Thus in the $n_0 = 64 \cdot 10^{18} \text{ m}^{-3}$ case a significant amount of neutrals are ionized by the filament, unlike in the $n_0 = 48 \cdot 10^{18} \text{ m}^{-3}$ case.

4.2. Dependence on detachment

Compared to the previous study, in attached conditions, the velocity of filaments in these higher density simulations is decreased [29]. Previously the slowest filament velocity reached was around 550 m/s at a target temperature of 0.8 eV . Higher target temperatures resulted in faster filament velocities. In the simulations presented here the target temperature does not drop below 2.5 eV , as the recombination acts as a heat source for the electrons at low temperatures. Fig. 9 shows the peak radial filament velocity versus the target temperature. While for the high target temperature cases

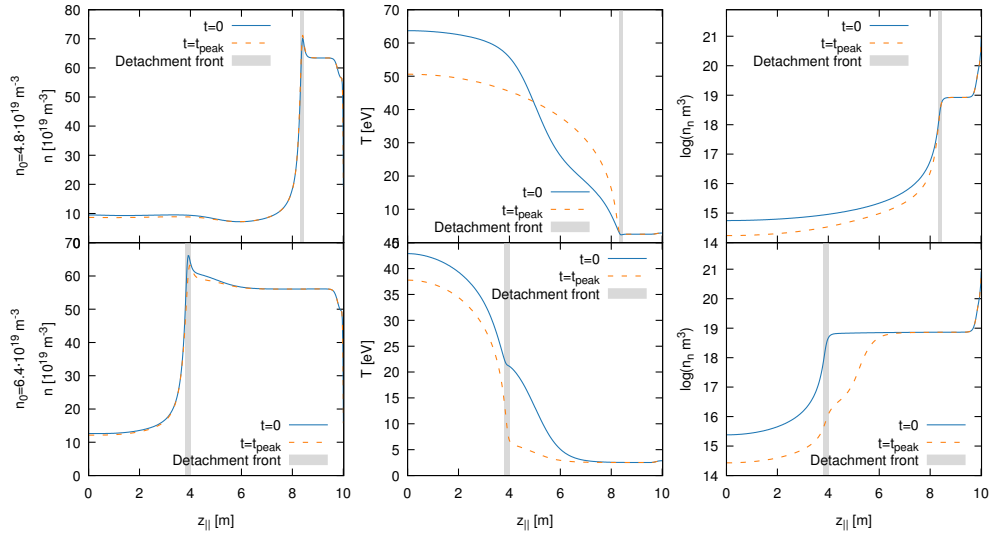


Figure 8: Plasma profiles at the centre of the filament. Shown in blue are the profiles just at the beginning of the simulation, before the neutrals could adjust to the perturbation. Shown in red are the profiles after $\approx 4 \mu\text{s}$. Shown is the plasma density (left), electron temperature (centre) and neutral density (right). On the top is the $n_0 = 48 \cdot 10^{18} \text{ m}^{-3}$ case, and on the bottom the $n_0 = 64 \cdot 10^{18} \text{ m}^{-3}$ case, both with 10 MW/m^2 energy influx, as shown in fig. 4(d,b). The detachment front is shaded in grey.

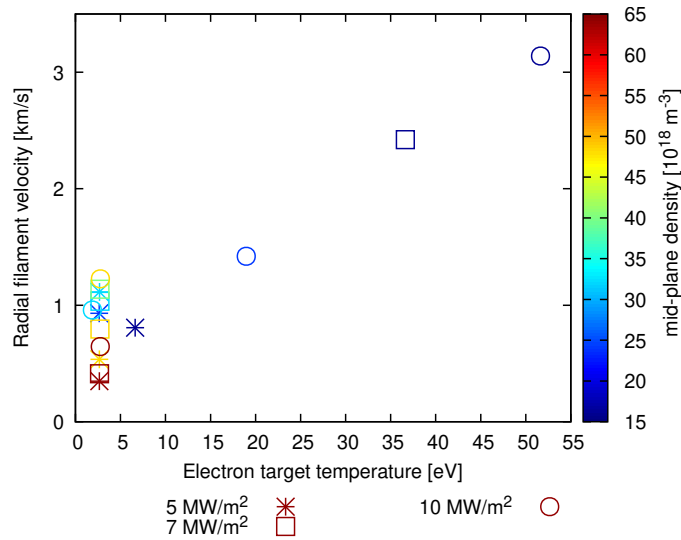


Figure 9: Peak radial filament velocity for the backgrounds shown in fig. 4 versus target temperature of the background. The target temperature dependency breaks down for target temperatures below 5 eV.

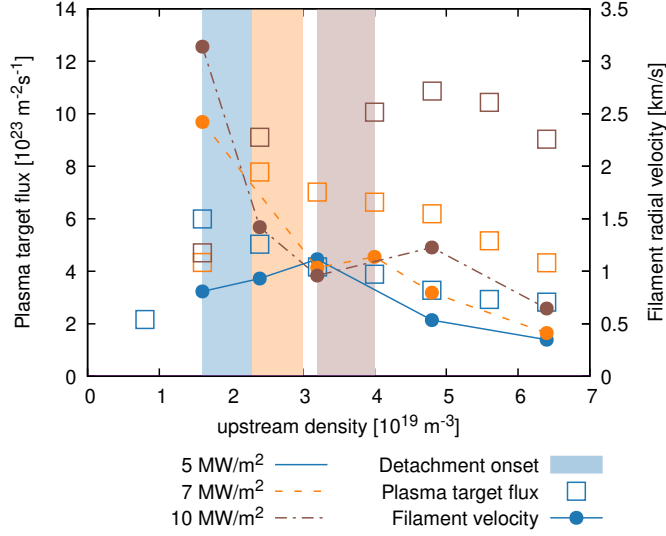


Figure 10: On the left axis is the particle target flux of the associated background profiles. On the right axis is the peak radial filament velocity for different plasma backgrounds. The lines are to guide the eye, and do not imply that the transition between the points would be linear. The shaded are represent detachment onset for the different energy influxes. A general decreasing trend of the radial velocity with increasing density is observed, except at the flux roll-over point, where the filaments become temporarily faster.

our previous findings of a target temperature dependence are reproduced [29], this does not hold for target temperatures below $\sim 5 \text{ eV}$. The main differences to the previous study is the increased plasma density, as well as the Franck-Condon energy source from ionisation.

To understand the dependence of the filament velocity in detached conditions, fig. 10 shows the filament velocity as a function of upstream density, as well as particle target flux of the associated backgrounds. The filament velocity generally decreases with increasing density. The 5 MW/m^2 case has an exception for densities less than $n_0 = 32 \cdot 10^{18} \text{ m}^{-3}$, the 7 MW/m^2 case between $n_0 = 32 \cdot 10^{18} \text{ m}^{-3}$ and $n_0 = 40 \cdot 10^{18} \text{ m}^{-3}$ and the 10 MW/m^2 case between $n_0 = 32 \cdot 10^{18} \text{ m}^{-3}$ and $n_0 = 48 \cdot 10^{18} \text{ m}^{-3}$. The particle target flux roll-over is at $n_0 = 16 \cdot 10^{18} \text{ m}^{-3}$, $n_0 = 24 \cdot 10^{18} \text{ m}^{-3}$ and $n_0 = 40 \cdot 10^{18} \text{ m}^{-3}$ respectively. In all three cases, with increasing density the target flux roll-over and pressure drop happen, and at even higher densities the radial velocity increases temporarily. This suggests that after detachment is reached, the filaments get faster, before the velocity begins to decrease again. At this point, a cold and dense plasma in front of the target is building up and with increased density as well as decreased temperature, the resistivity is significantly increased, which suppresses currents in the filament reaching the target. Fig. 11 shows the current density in the centre of the filament, for the 10 MW/m^2 cases. While in the attached cases, the currents flow to the target on the right hand side, in the detached cases the currents are only flowing to the edge of the cold plasma region, where strong currents due to the large density gradients are observed. The increase of the filament radial velocity with increased resistivity was predicted [24–26]. The decrease of the filament velocity with increasing density is at least partially due to a decreased drive as

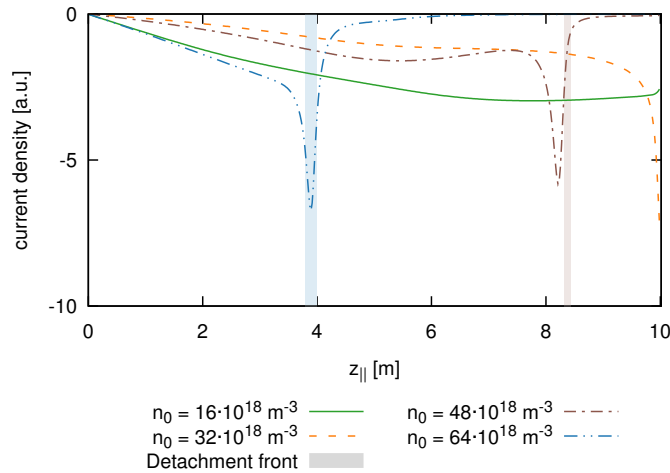


Figure 11: Current density at the centre of the filament after $\sim 4 \mu\text{s}$ for the 10 MW/m^2 cases shown in fig. 4(b,d,f,h). In the detached cases, currents near the target are strongly suppressed. The detachment front is shaded in the respective colour.

the temperature is decreased. In addition to an decreased drive, the plasma viscosity increases, which also reduces the filaments velocity. Thus in general the decreased drive and the increased viscosity are dominating over the increased parallel resistivity for most densities, with the exception after detachment is reached, where the velocities temporarily increase and the increased resistivity dominates over the other changes.

4.3. Dependence of critical size

The sink for the vorticity drive, and thus the dynamics of filaments strongly depends on the size of the filament with respect to the critical size δ^* . For small filaments, i.e. $\delta_{\perp} < \delta^*$, the vorticity is balanced mostly in the drift plane, and the filament velocity increases monotonically with size. For large filaments, the vorticity is balanced predominantly via parallel dynamics, and a monotonic decrease with filament size is expected.

To further understand the influence of detachment on filament dynamics, different sized filaments were seeded on the background profiles. The result of the filament size scan is shown in fig. 12. Also shown is the critical size, as determined by fitting a quadratic function in log-space using gnuplot [43]. Additionally to the full model, a second case is run where the perpendicular viscosity is set to zero. While the perpendicular diffusion constants are physically motivated, the real value is not known. Some models don't include viscosity or diffusion at all [18, 44]. The previous study found a strong viscosity dependence of the filament dynamics, thus the viscosity dependence was once more investigated. The neo-classical viscosity values were assumed to be the upper bound and setting the viscosity to zero is a natural lower bound. Thus the resulting error of this uncertainty is expected to be bound by the full model on one side, and by the no-viscosity case on the other hand.

In the filament size scan in attached conditions, the regime transitions from the viscous regime for small filaments to the sheath limited regime for large filaments,

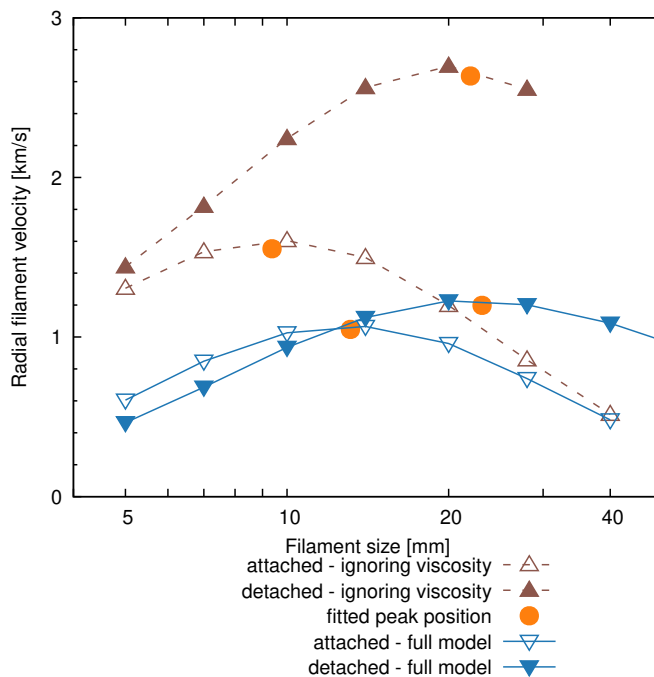


Figure 12: Peak radial filament velocity for different sized filaments. The blue, filled symbols are in detached conditions (10 MW/m^2 , $n_0 = 32 \cdot 10^{18} \text{ m}^{-3}$, fig. 4(f)), while the red, open symbols are in attached conditions (10 MW/m^2 , $n_0 = 48 \cdot 10^{18} \text{ m}^{-3}$, fig. 4(d)). The downward pointing triangles are from simulations using the full model, whereas the upward pointing triangles are from simulations ignoring the perpendicular viscosity. The fitted position of the critical size is shown as red dots.

where sheath currents are the main current closing mechanism. In detached conditions, for small filaments, the vorticity drive is mainly balanced by viscosity. For large filaments, sheath current can no further close the vorticity drive, as sheath currents are strongly suppressed, as shown in fig. 11. As mentioned earlier, the filament scaling expected for neutrals does not have a size dependence. As with increasing size the monotonic decrease is retained, while the high resistivity strongly reduces sheath currents, sheath currents are not fully suppressed. Looking at the contributions in the vorticity equation, it can be observed that the viscosity contribution is increasing for filaments until $\delta_{\perp} \approx 20 \text{ mm}$. While the viscosity contribution within the filament decreases with increasing size, the contribution at the detachment front shows a more complicated behaviour, as shown in fig. 13. While for small filaments the vorticity is balanced locally, for large ones the vorticity drive is advected towards the sheath, and as the viscosity is more effective at higher density and lower temperature, the viscosity still provides a significant closing mechanism at the front of the detached volume, but decreases quickly with increasing size due to the δ_{\perp}^{-2} dependence.

As the vorticity sink provided by viscosity is decreasing with increasing size, the impact of the neutrals is increasing. For the $\delta_{\perp} = 20 \text{ mm}$ filament, the neutrals contribution is roughly $\frac{1}{60}$ of the viscosity contribution, while in the $\delta_{\perp} = 40 \text{ mm}$ case the neutrals have nearly doubled their impact, and the neutrals contribution is

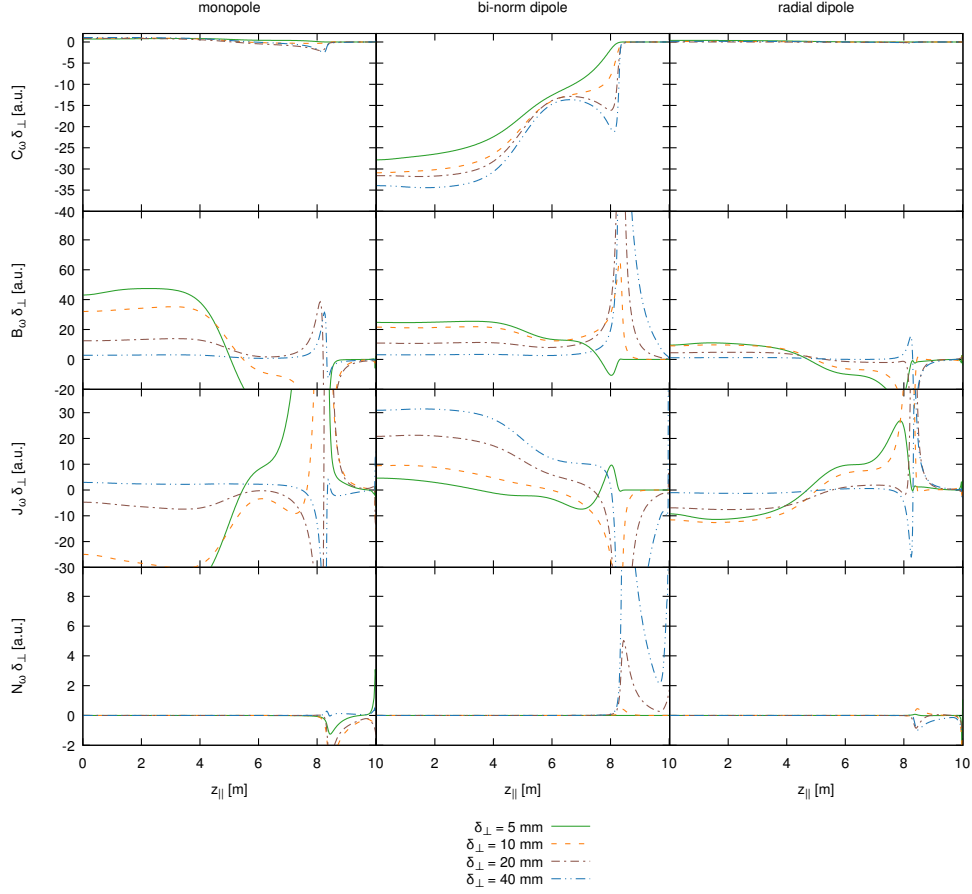


Figure 13: Contributions of the vorticity equation for the $n_0 = 48 \cdot 10^{18} \text{ m}^{-3}$ 10 MW/m^2 case for different sized filaments. The contributions are split in the base-functions discussed in sec. 2. The advective contribution isn't shown, as its magnitude is well below 3% of the other contributions.

about $\frac{1}{20}$ of the viscosity contribution.

In the full model, the filaments of 14 mm and larger are faster in the detached condition than in attached conditions. This is expected, as small filaments are not influenced by sheath currents, and the increased viscosity, $\mu_\omega \propto nT^{-\frac{1}{2}}$ as mentioned in eq. (14), resulting from the higher density in detached state will thus reduce the velocity the filament achieves. For large filaments, the suppression of sheath currents is much more important and the effect of viscosity is weaker, thus they are faster in detached conditions. In the case without viscosity, the filaments of all sizes, down to 5 mm are faster in the detached condition than in the attached case. This indicates that even for 5 mm filaments, in the absence of perpendicular viscosity, parallel dynamics plays a role, as a significant part of the vorticity drive is advected towards the target. In the low resistivity, attached case, sheath currents provide a monopole contribution, and the $E \times B$ term causes a significant contribution to the vorticity sink. In the high resistivity case, the $E \times B$ contribution is significantly reduced. In that case parallel advection and diffusion are preventing further acceleration of the filament. Therefore

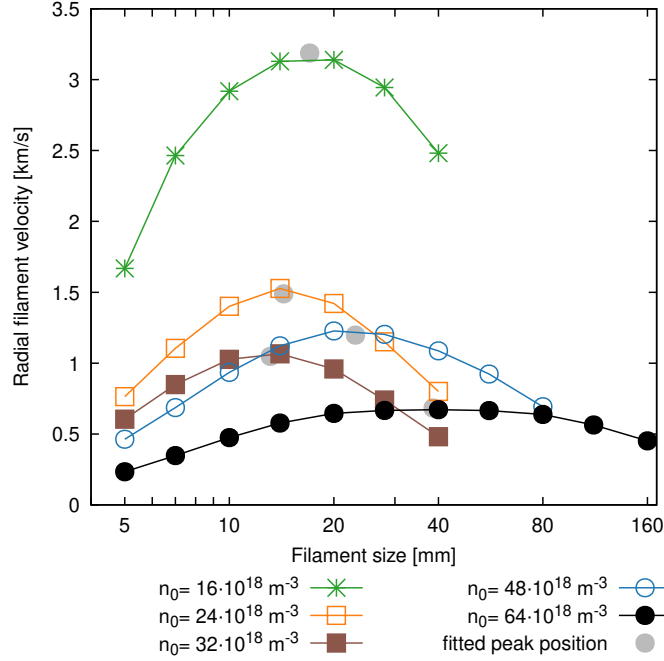


Figure 14: Peak radial filament velocity for different sized filaments for different backgrounds. The backgrounds have an energy influx of 10 MW/m^2 , and the densities range from $n_0 = 16 \cdot 10^{18} \text{ m}^{-3}$ to $n_0 = 64 \cdot 10^{18} \text{ m}^{-3}$.

in the absence of viscosity, even the small filaments are influenced by the sheath conditions, thus filaments of all sizes achieve higher velocities in detached conditions, where sheath effects are suppressed.

The full model as well as the no viscosity model shows an increase in velocity with detachment for larger filaments. Further, the critical size δ^* increases significantly with detachment. Note that δ^* is defined as the perpendicular size where filaments are fastest.

To put these results further into context, the scan has been extended to more densities, as shown in fig. 14. The density dependence of filaments of $\delta_{\perp} = 20 \text{ mm}$ has already been discussed in section 4.2. The trend is the same for larger filaments as well, while small filaments (10 mm and smaller) show a monotonic decrease with increasing density. In attached conditions the critical size δ^* decreases with increasing density. This is in contrast to our previous study, where an increase with increasing density was observed. The main difference between the two studies is, that here the energy influx was kept constant, whereas in the previous study, the upstream temperature was kept constant [29]. In the case of a fixed heat flux, an increased density results in an decreased temperature, due to pressure conservation. It seems thus that the decreasing temperature reduces the critical sizes stronger, then the density increases the critical size. As detachment is reached, the critical size δ^* shifts dramatically to larger sizes. This can be explained by the suppression of sheath currents, which allows larger filaments to reach higher velocities. As larger filaments are faster, the critical size is shifted towards larger sizes. Fig. 15 shows the plot of the critical size plotted against the respective density. The critical size was determined by fitting a quadratic

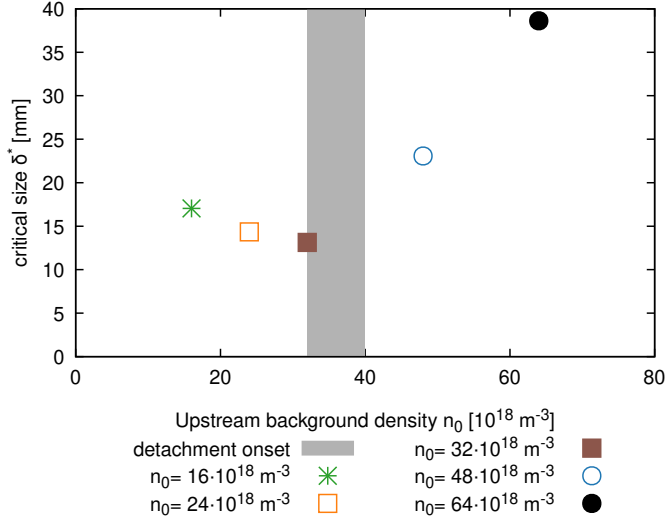


Figure 15: Critical size of the different densities shown in fig. 14. The shaded region denotes the onset of detachment. The backgrounds have an energy influx of 10 MW/m^2 , and the densities range from $n_0 = 16 \cdot 10^{18} \text{ m}^{-3}$ to $n_0 = 64 \cdot 10^{18} \text{ m}^{-3}$.

function against the radial velocity versus logarithm of the perpendicular size using gnuplot [43]. In the $n_0 = 64 \cdot 10^{18} \text{ m}^{-3}$ case the critical size is further increased with respect to the $n_0 = 48 \cdot 10^{18} \text{ m}^{-3}$ case, which is already detached. This demonstrates the importance of how far the detachment has moved upstream, which roughly linearly increases the collisionality integrated along the flux tube.

Based on these results, it is expected that for experimentally observed filaments in detached conditions are generally slower than in fully attached conditions, however not a simple relationship with detachment is expected, but rather filament size δ_{\perp} with respect to the critical size δ^* needs to be taken into account.

4.4. Rigidity of filaments

Filaments have been observed to bend in electro-magnetic models, where the pressure perturbation is not any more much smaller than the magnetic pressure [44]. The model used here however uses the electrostatic assumption, and in previous studies the filaments have been observed to be rigid. The radial displacement of the filaments seeded on the backgrounds shown in fig. 4 has been computed for the different x - y -slices along z_{\parallel} and is shown in fig. 16. In attached conditions, the velocity has no z_{\parallel} dependence, and the filament moves rigidly. Also in detached conditions, the filaments in $n_0 = 48 \cdot 10^{18} \text{ m}^{-3}$ 10 MW/m^2 as well as $n_0 = 32 \cdot 10^{18} \text{ m}^{-3}$ 5 MW/m^2 still move rigidly. Only the filaments in $n_0 = 64 \cdot 10^{18} \text{ m}^{-3}$ with 10 MW/m^2 and 5 MW/m^2 as well as $n_0 = 48 \cdot 10^{18} \text{ m}^{-3}$ 5 MW/m^2 show bending. In addition all showing a low radial velocity, the filaments that bend have in common that they were seeded partially within the detached region. This prevents currents within the filament to flow freely, which explains why the vorticity within the filament is strongly dependent on the position within the filament.

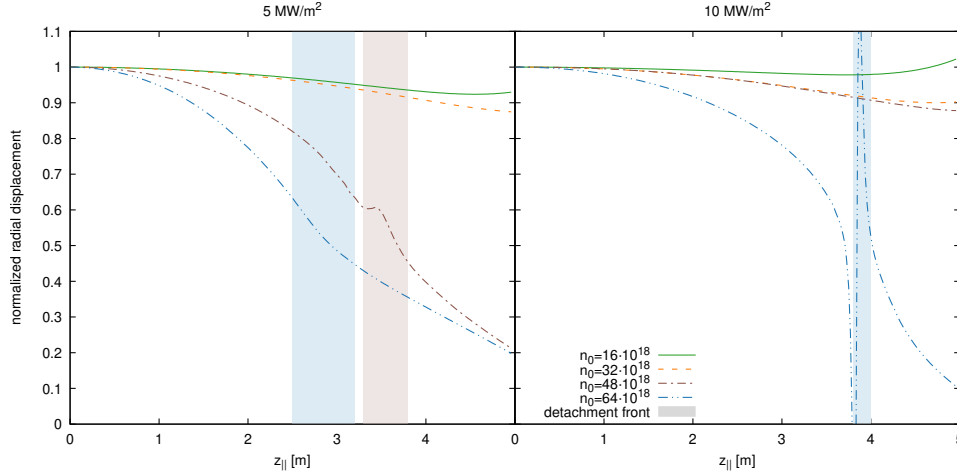


Figure 16: Dependence of the filaments radial displacement after $4 \mu\text{s}$ on the parallel direction z_{\parallel} for the different backgrounds in fig. 4. The displacement was normalized to the displacement at $z_{\parallel} = 0$. Note that only the upper half of the domain is plotted, where the filament was seeded. The detachment front is represented by a shaded area. In the $n_0 = 64 \cdot 10^{18} \text{ m}^{-3}$ 10 MW/m^2 case the detection did not work reliably around $z_{\parallel} \approx 4 \text{ m}$, as the background density features strong parallel gradients, thus small movements of the detachment front making the detection of the centre of the filament unreliable.

In fig. 16 the filaments that are in a detached region show significant bending. Around the detachment front, the filament has only move 60 % of the upstream value. Within the detached region, the retardation is even more prominent. The bended filaments are seeded on the backgrounds shown in fig. 4(a,b,c). Whilst this is an idealised scenario as the filaments are seeded partially within the detached region, the deviation of filaments from field alignment in detached plasmas may be a useful result for experimental comparison.

5. Discussion

Similar to the previous study, strictly in attached conditions, keeping the neutrals fixed at their background values has only a minor impact on the dynamics of filaments. If filaments are able to penetrate into a detached region, they can ionise significant amount of neutrals, which may be relevant to detachment burn-through studies, however. Burn-through is not studied in this paper, as the neutral code was unstable close to re-attachment.

Easy *et al* predicted that a cold divertor could increase the radial velocity of filaments, as well as the critical size δ^* due to a rise in collisional resistivity [25]. While both an increase in radial velocity as well as an increase of δ^* has been observed as detachment is reached, the increase of the radial velocity is rather weak, and a hotter divertor yields higher radial velocities in general. It has been suggested that detachment, or more generally a high collisionality in the divertor could be the cause of SOL flattening, as the high resistivity could prevent sheath currents, and thus increase the radial filamentary transport [45, 46]. This study shows that collisionality may be responsible for a change of filament dynamics, rather than e.g. the increased

neutral density. However, the increase of filament velocities with detachment is well below the radial velocities in sheath limited conditions, so this study does not support the hypothesis that shoulder formation is the result of high divertor collisionality and increased filament transport fluxes. The increase with detachment was significantly larger than the errors due to solver accuracy, finite discretisation or finite domain size effects, which were found to be below 2%.

Furthermore, as a high plasma density as well as a low plasma temperature is required to achieve a sufficiently high resistivity to sufficiently prevent sheath currents to influence the filament dynamics, this will most likely not be the case in the far SOL, thus even if the acceleration caused by detachment is higher than suggested by these simulations, the velocity should quickly drop, once the filament is connected to a lower density region and thus can connect to the target.

After detachment occurs, a strong increase of the critical filament size δ^* with increasing density is observed. In attached conditions a weak reduction of the critical size with increased density is observed, which is associated with a reduction of the temperature as the energy influx is kept constant. After detachment occurs, cold and dense plasma at the target is suppressing sheath currents, and with increasing density the detachment volume is increasing, thus shifting the critical size to larger values. While neutrals can partially compensate for the lack of sheath currents, the vorticity sink due to neutrals is over an order of magnitude smaller than the sink due to viscosity.

The observed filament bending agrees with Easy *et al* [25] where bending was observed if the resistivity was uniformly enhanced, whereas a localized resistivity at the target resulted in a rigid filament [25]. Note that this bending mechanism would only be expected in experiments, if the filament is within the cold, dense plasma region. The bending was only observed in cases where the detachment front has moved quite far upstream, and the filament was within the detached plasma.

Easy *et al* [25] increased the resistivity artificially by up to a factor of 10 000 and estimated that the temperature at the divertor would need to drop to 0.086 eV compared to the 40 eV reference case [25]. The estimates assumes that the resistivity has a temperature dependency $\nu_{\parallel} \propto T^{-3/2}$. However, the resistivity also has a density dependence i.e. $\nu_{\parallel} \propto n \cdot T^{-3/2}$. If we assume that the pressure $n \cdot T$ is preserved (same upstream conditions but colder divertor) the scaling can be expressed again in terms of the temperature: $\nu_{\parallel} \propto T^{-5/2}$. Thus achieving the 10 000 increase only requires 1 eV - which is much closer to the temperatures reached here and may explain why the bending effect is seen in the detached simulations.

While Easy *et al* [25] predicted that the velocity will be increased with increased resistivity, the self-consistent simulations conducted here show that the increase with detachment is significantly smaller, than the net decrease with respect to attached simulations, where target temperatures above 25 eV reach velocities exceeding 2 km/s - whereas in detached conditions only about 1 km/s was reached. However, a change in the transition of filament dynamics from inertial or viscous to sheath-limited is observed and the critical size of filaments δ^* increases dramatically after detachment. This is in agreement with experimental observation, that an increased collisionality does not result in an increase of the radial filament velocity [47]. Rather an increase of the filament size coincides with shoulder formation [47].

6. Summary

The paper presents attached as well as detached 1D parallel plasma profiles and the dynamics of filaments in a 3D slab geometry seeded on these profiles. The detachment features particle target flux roll-over as well as a significant plasma pressure drop. Detachment was achieved by using a refined neutral model, which is able to capture and evolve steep gradients in the neutral density, which is observed near the target.

In terms of dependence of the filament dynamics on the background conditions, a general decreasing trend of radial filament velocity with increasing plasma density is observed. This trend is temporarily broken as detachment is reached, where especially filaments larger than δ^* are faster than before detachment. This is caused by the higher parallel resistivity. This also causes an increase of the critical size, which further increases as the detachment front moves further upstream and the integrated resistivity increases.

While detachment can increase the radial velocity, the observed radial filament velocities in hotter, attached plasmas are still faster than the ones observed in detachment.

7. Acknowledgement

This work has been carried out within the framework of the EUROfusion Consortium and has received funding from the Euratom research and training programme 2014-2018 and 2019-2020 under grant agreement No 633053. The views and opinions expressed herein do not necessarily reflect those of the European Commission. This work used the EUROfusion High Performance Computer (Marconi-Fusion) through EUROfusion.

- [1] D'IPPOLITO, D. et al., *Physics of Plasmas* (1994-present) **18** (2011) 060501.
- [2] WALKDEN, N. et al., *Nuclear Materials and Energy* **12** (2017) 175 , *Proceedings of the 22nd International Conference on Plasma Surface Interactions 2016*, 22nd PSI.
- [3] SÁNCHEZ, E. et al., *Physics of Plasmas* **7** (2000) 1408.
- [4] ANTAR, G. Y. et al., *Phys. Rev. Lett.* **87** (2001) 065001.
- [5] GRAVES, J. P. et al., *Plasma Physics and Controlled Fusion* **47** (2005) L1.
- [6] GARCIA, O. et al., *Nuclear Fusion* **47** (2007) 667.
- [7] BOEDO, J., *Journal of Nuclear Materials* **390-391** (2009) 29 , *Proceedings of the 18th International Conference on Plasma-Surface Interactions in Controlled Fusion Device*.
- [8] KUBE, R. et al., *Plasma Physics and Controlled Fusion* **60** (2018) 065002.
- [9] BOEDO, J. A. et al., *Physics of Plasmas* **8** (2001) 4826.
- [10] CARRALERO, D. et al., *Nuclear Fusion* **58** (2018) 096015.
- [11] KUBE, R. et al., *Nuclear Materials and Energy* **18** (2019) 193 .
- [12] WALKDEN, N. et al., <https://github.com/boutproject/BOUT-dev/blob/master/examples/boutcore/blob2d.py>, Accessed 6 Mar 2019.
- [13] EASY, L. et al., *Physics of Plasmas* **21** (2014).
- [14] KRASHENINNIKOV, S., *Physics Letters A* **283** (2001) 368 .
- [15] GARCIA, O. et al., *Physics of Plasmas* (1994-present) **13** (2006) 082309.
- [16] THEILER, C. et al., *Phys. Rev. Lett.* **103** (2009) 065001.
- [17] KUBE, R. et al., *Physics of Plasmas* **18** (2011) 102314.
- [18] ANGUS, J. R. et al., *Phys. Rev. Lett.* **108** (2012) 215002.
- [19] JOVANOVIĆ, D. et al., *Physics of Plasmas* (1994-present) **15** (2008) 112305.
- [20] POTZEL, S. et al., *Nuclear Fusion* **54** (2014) 013001.
- [21] HUTCHINSON, I., *Nuclear Fusion* **34** (1994) 1337.
- [22] WISCHMEIER, M. et al., *Journal of Nuclear Materials* **390-391** (2009) 250 , *Proceedings of the 18th International Conference on Plasma-Surface Interactions in Controlled Fusion Device* *Proceedings of the 18th International Conference on Plasma-Surface Interactions in Controlled Fusion Device*.

- [23] COSTER, D., Journal of Nuclear Materials **415** (2011) S545 , Proceedings of the 19th International Conference on Plasma-Surface Interactions in Controlled Fusion.
- [24] KRASHENINNIKOV, S. I. et al., Journal of Plasma Physics **74** (2008) 679–717.
- [25] EASY, L. et al., Physics of Plasmas (1994-present) **23** (2016) 012512.
- [26] GARCIA, O. E., Plasma and Fusion Research **4** (2009) 019.
- [27] MILITELLO, F. et al., Nuclear Fusion **56** (2016) 104004.
- [28] MILITELLO, F. et al., Physics of Plasmas **25** (2018) 056112.
- [29] SCHWÖRER, D. et al., Plasma Physics and Controlled Fusion **61** (2018) 025008.
- [30] WALKDEN, N. R. et al., Plasma Physics and Controlled Fusion **58** (2016) 115010.
- [31] SCHWÖRER, D. et al., Nuclear Materials and Energy **12** (2017) 825 .
- [32] DUDSON, B. D. et al., Plasma Physics and Controlled Fusion **50** (2008) 124012.
- [33] DUDSON, B. D. et al., Journal of Plasma Physics **81** (2015).
- [34] WISING, F. et al., Contributions to Plasma Physics **36** 309.
- [35] DUDSON, B. D., <https://github.com/boutproject/SD1D/tree/master/doc>, 2017, Version 1538638; Accessed Sept 2018.
- [36] WESSON, J. et al., (2004).
- [37] FUNDAMENSKI, W. et al., Nuclear Fusion **47** (2007) 417.
- [38] MYRA, J. R. et al., Physics of Plasmas **13** (2006) 112502.
- [39] KUBE, R. et al., Physics of Plasmas **19** (2012) 042305.
- [40] MANZ, P. et al., Physics of Plasmas **20** (2013) 102307.
- [41] EASY, L., *Three Dimensional Simulations of Scrape-Off Layer Filaments*, PhD thesis, University of York, 2016.
- [42] DUDSON, B. D. et al., <https://github.com/boutproject/BOUT-dev>, BOUT++, 2019.
- [43] WILLIAMS, T. et al., Gnuplot 5.0: an interactive plotting program, <http://gnuplot.sourceforge.net/>, 2016.
- [44] LEE, W. et al., Journal of Nuclear Materials **463** (2015) 765 , PLASMA-SURFACE INTERACTIONS 21.
- [45] CARRALERO, D. et al., Nuclear Materials and Energy **12** (2017) 1189 , Proceedings of the 22nd International Conference on Plasma Surface Interactions 2016, 22nd PSI.
- [46] KUANG, A. et al., Nuclear Materials and Energy **19** (2019) 295 .
- [47] VIANELLO, N. et al., Nuclear Fusion **60** (2019) 016001.
- [48] TANGE, O., *GNU Parallel 2018*, Ole Tange, 2018.